Nationaal Lucht- en Ruimtevaartlaboratorium
National Aerospace Laboratory NLR

NLR-TP-2001-321

Accurate computation of drag for a wing/body configuration using multi-block, structured-grid CFD technology

O.J. Boelens, M. Laban, C.M. van Beek and R. van der Leeden

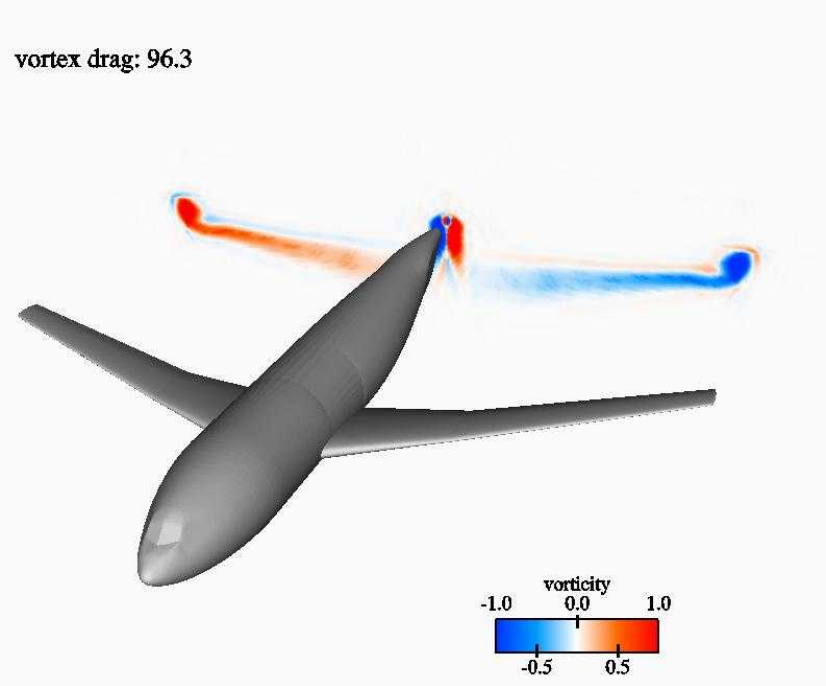

Nationaal Lucht- en Ruimtevaartlaboratorium
National Aerospace Laboratory NLR

NLR-TP-2001-321

Accurate computation of drag for a wing/body configuration using multi-block, structured-grid CFD technology

O.J. Boelens, M. Laban, C.M. van Beek and R. van der Leeden*

* *University of Twente (Enschede, the Netherlands)*

This report is based on a presentation held at the AIAA CFD Drag Prediction Workshop, Anaheim, CA, USA, 9-10 June 2001.

Division:	Fluid Dynamics
Issued:	July 2001
Classification of title:	Unclassified

Summary

In this report the contribution of the National Aerospace Laboratory NLR to the 'CFD Drag Prediction Workshop' organized by the AIAA in Anaheim, CA, on June 9-10, 2001, is presented. This contribution consists of both the results of all test cases and a discussion on the accurate computation of drag coefficients. Two approaches are presented and discussed. The first method performs a grid convergence study using a sequence of nested grids yielding the grid-converged drag coefficient. To enable this study to be carried out, such a sequence of nested multi-block structured grids ('NLR' grid) has been generated. The second method, using one grid only, decomposes the drag coefficient into its 'physical components' (vortex, wave and viscous drag). As a consequence, this method provides the aerodynamic designer with a helpful tool, because of its diagnostic potential.

Contents

(42 pages in total)

List of figures

List of tables

This page is intentionally left blank.

Nomenclature

Symbols

$c_{1,2,3}$	Extrapolation constants
C_D	Drag coefficient
$C_{D_{h=0}}$	Grid-converged drag coefficient
$C_{D_{entropy}}$	Entropy drag coefficient
$C_{D_{friction}}$	Friction drag coefficient
$C_{D_{far\text{-}field}}$	Drag obtained by 'far-field approach'
$C_{D_{pressure}}$	Pressure drag coefficient
$C_{D_{viscous}}$	Viscous drag coefficient
$C_{D_{vortex}}$	Vortex drag coefficient
$C_{D_{wave}}$	Wave drag coefficient
C_L	Lift coefficient
C_M	Pitching moment coefficient
h	Relative mesh size
k	Turbulent kinetic energy
L_{ref}	Reference length
M_∞	Free-stream Mach number
$\overline{n}$	Normal
R	Gas constant
S_t	Area of 'Trefftz plane'
S_{ref}	Reference area
U_∞	Free-stream velocity
$\overline{U}$	Velocity vector
$x_{Trefftz}$	Location of 'Trefftz plane'
y^+	Dimensionless, sublayer-scaled distance

Greek symbols

α	Angle of attack
γ	Specific heats ratio
Δs	Entropy increase relative to free-stream condition
ϕ	Potential function
ρ	Density
ρ_∞	Free-stream density
τ	Turbulence time scale ($= 1/(\omega + \omega_0)$)

ω	Specific dissipation rate
Ω	Flow field domain
ψ	Stream function
ζ	Vorticity

1 Introduction

The objectives of the AIAA CFD Drag Prediction Workshop are:

- to assess the state-of-the-art computational methods as practical aerodynamic tools for aircraft force and moment prediction,
- to provide an impartial forum for evaluating the effectiveness of existing computer codes and modeling techniques using Navier-Stokes solvers, and
- to identify areas needing additional research and development.

This report presents the contribution of the National Aerospace Laboratory NLR to this workshop. The focus of this report is on the extraction of the grid-converged drag coefficient from grids with finite mesh widths. Two complementary approaches, i.e. a grid convergence study using a sequence of nested grids and a breakdown analysis of the drag into its 'physical' components, will be discussed.

1.1 Outline of the report

In the next section, the flow solver ENSOLV, which is part of NLR's flow simulation system ENFLOW, is outlined. The governing equations (including the turbulence model), the spatial discretization, the boundary conditions and the solution procedure will be discussed. Next, two methods to obtain the aerodynamic drag are outlined. The first method computes the grid-converged drag by extrapolation using a sequence of nested grids. The second method decomposes the drag into its three 'physical' components.

In addition to the 'DPW' grid which has been provided by the 'AIAA Drag Prediction Workshop', a multi-block structured grid ('NLR' grid) has been generated. A complete section is dedicated to the description of this grid. Both the topology and the grid are discussed. This discussion is followed by a description of the test cases and the results obtained. The results on the 'DPW' grid are for a number of cases compared with those on the 'NLR' grid. Furthermore, a comparison with experimental data is provided. In addition, the methods to obtain the grid-converged drag are illustrated. Finally, concluding remarks are made.

2 CFD method

In this section a brief description of the flow solver ENSOLV, which is part of NLR's flow simulation system ENFLOW, is given. The flow solver ENSOLV is capable of solving the Euler and Navier-Stokes equations on multi-block structured grids for arbitrary configurations. The present simulations have been performed with version 4.10 of the flow solver ENSOLV. For more details on the flow solver ENSOLV, see Ref. 4.

2.1 Reynolds-averaged Navier-Stokes equations and turbulence model

The flow solver ENSOLV employs the time-dependent Reynolds-averaged Navier-Stokes equations which are integrated in (pseudo) time towards a steady-state solution. The equations are cast into the full conservation form employing the density ρ, the components of the momentum vector $\rho\mathbf{u}$ and the total energy per unit volume ρE as dependent variables. The equations are non-dimensionalized using the free-stream static pressure, the free-stream density, the free-stream temperature and a reference length (for example the aerodynamic mean chord).

Several turbulence models (Cebeci-Smith, Baldwin-Lomax, Johnson-King, k-ω) are implemented to model the turbulent stress and heat flux term appearing in the equations due to the averaging process. In the present simulations the k-ω two-equation turbulence model has been used. The model used is basically the original model as proposed in Ref. 9. The equations are, however, slightly modified by the introduction of a 'cross diffusion' term, as proposed in Ref. 10. This modification has been introduced to resolve the dependency on the free-stream value of ω(see Ref. 3).

2.2 Spatial discretization

The equations are discretized in space using a cell-centered, central-difference, finite volume scheme. For each grid cell of the structured (multi-block) computational grid, the equations are integrated over the cell volume requiring only the evaluation of convective and viscous fluxes at the cell surface.

In order to prevent odd-even decoupling in the solution, fourth-order artificial dissipation terms have been added to the equations (Ref. 4). A second-order artificial dissipation term has been added for good shock wave capturing. This second-order artificial dissipation term is switched on near shock waves dependent on the computed value of a shock sensor. The artificial dissipation terms are in each grid cell scaled with a term depending on the aspect ratio of the grid cell. Finally, the scalar formulation of the dissipation as described above can be replaced by a matrix formulation (Ref. 4). Matrix dissipation can be independently employed in all three grid directions. For the simulations presented in this report, the default formulation of the flow solver has been used,

i.e. matrix dissipation is employed in the 'surface normal' direction and scalar dissipation in the other two directions.

2.3 Boundary conditions

In the simulations the following boundary conditions have been employed:

- At the far-field boundaries, a free-stream boundary condition based on Riemann invariants of the locally linearized one-dimensional Euler equations has been used. Since the flow at these boundaries is subsonic, the value of the 'incoming' Riemann invariants is computed using the free-stream values. The remaining invariants are extrapolated from the computational domain.
- At the wing and the body, the viscous flow condition of no-slip (Navier-Stokes adiabatic solid wall) is employed.
- At the symmetry plane, a symmetry boundary condition has been used. For the boundary condition used, the grid has not necessarily to be orthogonal to the symmetry plane.
- At the two faces coming from the wing trailing edge (see section 5) a smooth internal face condition for pairs of external faces has been used.

For the k-ω turbulence model, the following procedure has been used. To remove the singular behavior of ω at the solid walls, the equations of the k-ω model are reformulated such that instead of ω the quantity $\tau = 1/(\omega + \omega_0)$ is used. Here ω_0 is a positive constant (default value $\omega_0 L_{ref}/U_\infty = 20$, with U_∞ the free-stream velocity and L_{ref} the reference length). At the solid boundaries, i.e. the wing and the body, both k and τ are set to zero. For the turbulence equations, no specific transition point has been prescribed, as required for the workshop. The k-ω model is used in the first layer of blocks surrounding the geometry, see section 5. To prevent unphysical high values of k near stagnation points, the production term in the k-equation has been limited to a maximum of 20 times the dissipation term in the k-equation.

At the 'inflow' parts of the far-field boundary, the free-stream values of the turbulent variables are computed from the free-stream turbulent Reynolds number (0.01 in the present simulations) and the free-stream dimensionless turbulent kinetic energy ($k/U_\infty^2 = 10^{-6}$ in the present simulations).

2.4 Solution procedure

Employing the discretization scheme as described above, a time-dependent system of ordinary differential equations results. This system of equations is integrated towards a steady-state solution by an explicit Runge-Kutta scheme. To increase convergence, local time stepping and residual averaging may been used. Finally, convergence may be accelerated by a multi-grid scheme using a W-cycle with 5 pre- and post-relaxations on each of the multi-grid levels.

3 Grid convergence strategy

For non-linear CFD codes, like the flow solver ENSOLV, it is not possible to establish global error estimates a priori. This observation holds even for the specification of the order of accuracy in terms of a representative mesh size h. The numerical algorithm incorporated in the flow solver ENSOLV is locally second-order accurate, except in specific regions near shock waves and near strong grid non-uniformities where it is first-order accurate. Hence, the algorithm features a mix of first- and second-order accuracy.

In the absence of a global error estimate, it is assumed that for some neighborhood $0 < h < h_{max}$, the global accuracy of the CFD solution on a family of successively refined grids depends on the relative mesh size h. The total drag coefficient computed on such a sequence of nested grids can be represented either by a quadratic extrapolation

$$C_D(h) = C_{D_{h=0}} + c_1 h + c_2 h^2 \tag{1}$$

or by

$$C_D(h) = C_{D_{h=0}} + c_3 h^{\frac{3}{2}} \tag{2}$$

where c_1 through c_3 denote extrapolation constants and $C_{D_{h=0}}$ is the configuration drag coefficient for vanishing mesh width.

The strategy is to solve the Navier-Stokes equations on three different grids for application of Eq. 1, or on two different grids for application of Eq. 2, such that these equations allow the constants (including the grid-converged values $C_{D_{h=0}}$) to be calculated. The combination of the grids and the extrapolation method used is given in Tab. 1. The required sequence of nested grids

Equation	1	1	2	2
h=4-grid	●	-	-	-
h=2-grid	●	●	●	-
h=4/3-grid	-	●	-	●
h=1-grid	●	●	●	●

Table 1 Grid levels used for grid convergence study.

as displayed in Tab. 1 is best generated through successive grid coarsening of an initial 'fine' grid, such that the successive grids feature constant characteristics in terms of the cell angles, cell aspect ratios and cell stretchings. Therefore, a computational grid (h=1) of sufficient quality is generated first. The h=2-grid is produced by deleting alternately grid points from the h=1-grid. The h=4-grid is produced in the same manner from the h=2-grid. An 'intermediate' (h=4/3) grid belonging to

the same family (cell angles, cell aspect ratios and cell stretchings) is generated directly by the grid generator using $3/4$ of the number of grid points in each direction compared to the h=1-grid. Application of Eq. 1 using the h=4-grid holds the risk that the main flow features, such as shock waves, are insufficiently resolved on the h=4-grid.

4 Total drag breakdown

An alternative approach to drag calculation, using only one grid level, is the so-called 'far-field approach' instead of the (near-field) surface integration. Following this 'far-field approach' and making some simplifying assumptions, one can decompose aerodynamic drag into its three 'physical' components, i.e. induced or vortex drag (due to trailing, streamwise vorticity), viscous drag (due to turbulent dissipation in boundary layers and wakes) and wave drag (due to viscous dissipation in shock waves). In addition to these drag components also spurious drag, which is neither vortex drag, viscous drag or wave drag, may be present. The combination of viscous drag, wave drag and spurious drag is referred to as entropy drag. It is observed that aerodynamic designers generally favor this 'far-field approach' because of its diagnostic potential.

The calculation procedure is as follows (see also Refs. 2, 5 and 7). First, the total drag is split into its vortex and entropy drag components. The vortex (induced) drag, which is associated with the generation of lift, can be computed by observing the vorticity component parallel to the free-stream velocity vector on a so-called 'Trefftz plane' (denoted by S_t) located at some distance downstream of the configuration. A vortex drag algorithm based on the vorticity (ζ)-streamfunction (ψ) formulation is used, because the vorticity is non-zero in only a limited area of the 'Trefftz plane' and therefore the integration is to be performed only over this limited area. Also the value of the vorticity/stream function integral is fairly insensitive to the exact streamwise location of the 'Trefftz plane'. Thus the vortex drag coefficient can be computed from

$$C_{D_{vortex}} = \frac{1}{S_{ref}} \int_{S_t} \frac{\psi}{U_\infty L_{ref}} \frac{\zeta}{U_\infty / L_{ref}} dS$$

Since the entropy drag integral over the 'Trefftz plane' does not allow to distinguish between wave drag, viscous drag and spurious drag, a methodology has been derived to enable the computation of each of the three drag types. This is accomplished by the transformation of the surface integral over the 'Trefftz plane' into a volume integral over the flow field domain Ω in the following divergence form

$$C_{D_{entropy}} = \frac{2}{\gamma M_\infty^2 S_{ref}} \int_\Omega \overline{\nabla} \left[f\left(\frac{\Delta s}{R}\right) \frac{\rho}{\rho_\infty} \frac{\overline{U} \cdot \overline{n}}{U_\infty} \right] d\Omega$$

with

$$f\left(\frac{\Delta s}{R}\right) = \frac{\Delta s}{R} + \frac{1 + (\gamma - 1) M_\infty^2}{2\gamma M_\infty^2} \left(\frac{\Delta s}{R}\right)^2$$

This volume integral can be evaluated in Ω on a cell by cell basis. In these equations Δs denotes the entropy increase relative to free-stream condition, R the gas constant and γ the specific heats ratio. An automated zonal detection algorithm is used to assign the drag resulting from each cell

to either the wave drag, the viscous drag or the spurious drag. If the value of a shock sensor (based on the local velocity vector and the local pressure gradient) exceeds the threshold value for shock wave cells, the entropy production in the grid cell is assigned to the wave drag. On the other hand, the entropy production in a grid cell is assigned to the viscous drag if the value of a viscous sensor (based on the dissipation function associated with the fluid viscosity) exceeds the threshold value for boundary layer and wake cells. Finally, if the entropy production in a grid cell can not be assigned to the wave drag or the viscous drag, it is assigned to the spurious (or non-physical) drag. This spurious drag is not added to the total drag balance and in this way the contribution of numerical errors resulting from the flow solver is left out. In this way, this method presents a complementary approach to the grid convergence strategy described in section 3.

The above described drag classification algorithm has been coded into the code AIRDRAG, Ref. 2, which interfaces to the various block-structured, unstructered and hybrid flow solvers by reading in the data (state vector) of the 3D flow field in TECPLOT format.

5 Computational grid

5.1 Topology

For test cases two, three and four (see section 6, a multi-block structured grid has been generated using the domain modeler ENDOMO and the grid generator ENGRID, both part of the ENFLOW CFD system. The overall topology of this so-called 'NLR' grid is an O-O-topology.

The topology around the DLR-F4 wing/body configuration consists of three layers of blocks. The first layer of blocks has been generated using the 'off-set' method. This method automatically creates a block by translating a surface patch (36 in total for the present wing/body configuration) in the surface normal direction over a specified off-set distance. The off-set distance has been taken relatively large, i.e. 50 mm or 0.354 aerodynamic mean chord lengths. The off-set distance has been taken this large in order to minimize the effect of block boundaries, which are a potential source of numerical errors, on the computation of the aerodynamic drag coefficients. See Fig. 1(a) for the resulting block decomposition. This layer of blocks comprises the viscous boundary layer around the configuration. During the surface grid generation process, the open trailing edge of the wing has been closed at the fuselage and at the wing tip to simplify the topology generation. In contrast to the 'DPW' grid, the faces leaving the trailing edge converge into one edge.

Both the second and the third layer of blocks have been generated using the 'potential' method. This method can be best explained by considering the electrostatic field that is generated by two perfectly conducting closed surfaces, featuring different constant electric potential values. One of the surfaces coincides with the surface of the aircraft configuration, whereas the other surface is the far-field bounding box, which entirely encloses the aircraft configuration. A potential problem is defined by introducing ϕ as a harmonic function satisfying the Laplace equation. The solution of the Laplace equation yields the potential function ϕ. Next, the electric field-lines are calculated by taking the gradient of ϕ. These field-lines can be considered as block-edges. For more details of this method, see Ref. 8. In order to obtain a smooth convex shape for the exterior surface of the second layer of blocks, four blocks are added to the first layer of blocks to make the shape of the exterior surface of this layer of blocks more convex, see Fig. 1(b). The obtained topologies are illustrated in Figs. 1(c) and 1(d). The resulting topology around the DLR-F4 wing/body configuration consists of 104 blocks; whereas the distance from the configuration to the far-field boundary equals 38 aerodynamic mean chord lengths.

5.2 Grid

Using the above described O-O-topology, a grid has been generated with the grid generator ENGRID, part of the ENFLOW CFD system. The first layer of blocks, i.e. the layer used for the viscous boundary layer computation, contains 40 grid points in the surface normal direction. The

width of the first grid cell in the surface normal direction is 0.0014 mm. This value was found to be sufficient to guarantee a value of y^+ equal to one. The number of grid points in the boundary layer turned out to be approximately 30. The maximum growth rate of the cell width in this layer of blocks in the surface normal direction equals 1.3. The second and third layer of blocks both have 24 grid points in the surface normal direction.

The resulting grid (see Figs. 2(a)-2(b) for details of the grid in the symmetry plane and around the configuration nose) contains $2,840,576$ grid cells. This grid is referred to as the h=1-grid. In order to perform a grid convergence study (see section 3) additional grids have been created by alternately deleting grid points from the h=1-grid. In this way, a h=2-grid containing $355,072$ grid points and a h=4-grid containing $44,384$ grid points have been generated. In addition, an 'intermediate' grid, referred to as the h=4/3-grid and characterized by the same cell angles, cell aspect ratios and cell stretchings as for the other grids, has been generated directly by the grid generator using $3/4$ of the number of grid points in each direction compared to the h=1-grid. This 'intermediate' grid contains $1,198,368$ grid points.

6 Test cases

Flow field simulations have been performed for the DLR-F4 wing/body configuration. These simulations include

(i) a single point simulation ($M_\infty = 0.75$ and $C_L = 0.500 \pm 0.001$) (test case one),

(ii) drag polar simulations for $M_\infty = 0.75$ and α=$-3°$,$-2°$,$-1°$,$0°$,$1°$,$2°$ (test case two),

(iii) constant-C_L-Mach-sweep simulations for $C_L = 0.500 \pm 0.001$ (test case three) and

(iv) simulations to obtain the drag rise curve for $C_L = 0.400 \pm 0.001$, $C_L = 0.500 \pm 0.001$ (i.e. identical to test case three) and $C_L = 0.600 \pm 0.001$ (test case four).

For all simulations, the Reynolds number Re based on the aerodynamic mean chord equals $3 \cdot 10^6$. An overview of the simulations for test case one, three and four is given in Tab. 2.

The simulation for test case one has been performed on the 'DPW' grid which has been provided by the 'AIAA Drag Prediction Workshop'. The simulations for test cases two, three and four have been performed on the 'NLR' grid described in section 5. However, to compare the results obtained with the 'DPW' grid and the 'NLR' grid, test case one has also been performed using the 'NLR' grid, whereas test case three also has been performed using the 'DPW' grid.

During all simulations, grid sequencing has been used. For the simulations on the 'DPW' grid (test case one and three), 1000 iterations are performed on the h=2-grid at a fixed angle of attack. The results of this simulation are input to the simulation on the h=1-grid using the same fixed angle of attack. On this grid 500 iterations have been performed. Finally, a constant-C_L simulation using 1000 iterations is done on the h=1-grid using the results of the h=1-grid simulation with a fixed angle of attack as initial condition. The simulations on the 'NLR' grid (case one to four) start with 1500 iterations on the h=4-grid using a fixed angle of attack. Next, the simulation is continued at the same fixed angle of attack on the h=2-grid for 600 iterations. Then, a simulation on the h=1-grid is performed. On this grid 600 iterations have been performed. Finally, for test case one, three and four, a constant-C_L simulation is carried out on the h=1-grid using the results of the h=1-grid simulation with the fixed angle of attack as initial condition. For this simulation 1200 iterations have been used.

In addition to the above described test cases, a grid convergence study and a total drag breakdown analysis have been performed for $M_\infty = 0.75$ and $\alpha = 0°$. For the grid convergence study using the 'NLR' grid an additional simulation on the h=4/3-grid has been performed (see also section 3). For the simulation on this grid 1250 iterations have been used.

For all simulations, local time stepping, multi-grid and residual averaging has been used to accelerate convergence. On both the 'DPW' grid and the 'NLR' grid, converged solutions were obtained with the above given numbers of iterations.

The present simulations have been performed on the NLR NEC SX-5/8B parallel vector super-computer with 64GByte memory, using one processor.

7 Results

7.1 General results

The results of the single point ($M_\infty = 0.75$ and $C_L = 0.500 \pm 0.001$) simulation on the 'DPW' grid and the 'NLR' grid (h=1) are shown in Tab. 3. The total drag coefficient obtained on the 'DPW' grid is 13.9 drag counts higher than that obtained on the 'NLR' grid (h=1). This difference is mainly due to a higher (12.5 drag counts) pressure drag coefficient on the 'DPW' grid. The friction drag coefficient differs slightly on both grids (only 1.4 drag counts).

Tab. 4 summarizes the results of test case two, i.e. the drag polar simulations for $M_\infty = 0.75$. In Figs. 3(a)-3(c), the results are compared with results of the experiments on the DLR-F4 wing/body configuration performed in the NLR-HST wind tunnel (see Ref. 1). The agreement of the experimental and numerical results is generally fair. The C_L-C_D-curve shows good agreement. Note that the data point for which the free-stream Mach number M_∞ equals 0.75 and the angle of attack α equals $0°$ is used to apply the grid convergence study (section 3) and the total drag breakdown analysis (section 4), see section 7.2.

	C_L		
M_∞	0.400 ± 0.001	0.500 ± 0.001	0.600 ± 0.001
0.50	●	○ ●	●
0.60	●	○ ●	●
0.70	●	○ ●	●
0.75	●	◇ ○ ●	●
0.76	●	○ ●	●
0.77	●	○ ●	●
0.78	●	○ ●	●
0.80	●	○ ●	●

Table 2 Matrix containing test cases one (◇), three (○) and four (●).

The results (both on the 'NLR' grid and the 'DPW' grid) of the constant-C_L-Mach-sweep ($C_L = 0.500 \pm 0.001$) simulations, i.e. test case three, are displayed in Tab. 5. This table shows that the total drag coefficients obtained on the 'DPW' grid for all conditions exceed the drag coefficients obtained on the 'NLR' grid. The difference is increasing with increasing Mach number. The higher total drag values on the 'DPW' grid are mainly due to a higher pressure drag values on this grid.

Finally, the results of test case four (drag rise curve for $C_L = 0.400, 0.500$ and 0.600 ± 0.001) are shown in Tabs. 6-8. These simulations have been performed on the 'NLR' grid (h=1).

7.2 Grid convergence study and total drag breakdown for $M_\infty = 0.75$ and $\alpha = 0°$

The data point ($M_\infty = 0.75$, $\alpha = 0°$) has been further explored performing both a grid convergence study (section 3) and a total drag breakdown analysis (section 4).

The combinations of the grids and the extrapolation method used for the present grid convergence study are shown in Tab. 1. Tab. 9 shows the total drag coefficients as well its two components, the pressure drag coefficient and the friction drag coefficient, on the sequence of grids ('DPW' grid, h=2 and 1 and 'NLR' grid, h=4, 2, 4/3 and 1). The values obtained from grid extrapolation (h=0) are shown in Tab. 10. These results are also depicted in Figs. 4(a)-4(b), showing the total drag coefficient as function of the relative mesh size h. Tab. 10 shows that the extrapolated values (h=0) on the 'NLR' grid, resulting from the two extrapolations (Eqs. 1 and 2) and various sequences of grid sizes, agree very well. The difference between the highest and the lowest extrapolated value is only 1.6 drag counts. The extrapolated value using the 'DPW' grid (h=1 and 2) is approximately 7 drag counts higher than the values using the 'NLR' grid.

The results of the total drag breakdown analysis computed by the code AIRDRAG on the 'DPW' grid (h=1) and the 'NLR' grid (h=1) are shown in Tab. 11. Two downstream locations for the 'Trefftz plane' have been used, i.e. $x_{Trefftz} = 1250$ mm (0.411 aerodynamic mean chord lengths behind the plane) and $x_{Trefftz} = 2400$ mm (8.55 aerodynamic mean chord lengths behind the plane), in order to investigate the influence of this location on the results, in particular the influence of numerical dissipation of vorticity for increasing downstream location. Figs. 5(a)-5(f) ('DPW' grid (h=1)) and 6(a)-6(f) ('NLR' grid (h=1)) present for both location of the 'Trefftz plane' the distribution of the non-dimensional streamwise vorticity over the 'Trefftz plane' (upper figures), the grid cells which are identified as shock wave cells by the shock sensor at a number of stations on the wing, including the level of entropy increase with respect to free-stream $\Delta s/R$ in each cell (middle figures), and the grid cells which are identified as viscous cells (both in the boundary layer and in the wake) by the viscous sensor at the spanwise stations on the wing (lower figures). Regarding these figures the following remarks can be made:

- The vorticity is dissipated faster in the 'NLR' grid having an O-O-topology than in the 'DPW' grid having an H-H-topology (compare Figs. 5(a)-5(b) and 6(a)-6(b) for $x_{Trefftz} = 2400$ mm), resulting in a larger decrease of the vortex drag when moving the 'Trefftz plane' from $x_{Trefftz} = 1250$ mm to $x_{Trefftz} = 2400$ mm (17.1 drag counts on the 'NLR' grid vs. 10 drag counts on the 'DPW' grid).
- The wave drag found using the 'DPW' grid is slightly higher than that found using the 'NLR' grid (2.0 and 1.9 drag counts vs. 1.0 drag count, respectively). The 'DPW' grid results, however, show some spurious wave drag contributions at the block boundaries above the wing.

- The viscous drag computations show a variation of 1.9 drag counts on the 'DPW' grid and 10.3 drag counts on the 'NLR' grid. Both grids suffer from spurious viscous drag contributions in the wake region. For the 'DPW' grid also some spurious contributions to the viscous drag at the block boundaries above the wing are present.

The total drag obtained by this 'far-field approach', i.e. $C_{D_{far\text{-}field}}$, equals 297.8 drag counts on the 'DPW' grid (h=1) and 295.2 drag counts on the 'NLR' grid (h=1) when using $x_{Trefftz} = 1250$ mm, i.e. the solutions with the least amount of vorticity dissipation. These values are higher than those obtained from the grid convergence study (7.4 drag counts higher on the 'DPW' grid and $11.1 - 12.7$ drag counts higher on the 'NLR' grid). It should, however, be noted that the 'NLR' grid is more suited for a grid convergence study based on near-field data than for a 'far-field approach', due to its O-O-topology, which clusters the grid points around the aerodynamic configuration. Applying this 'far-field approach' to a sequence of nested grids, it yields the same grid-converged drag results for consistent RANS solvers.

8 Concluding remarks

In this report the contribution of the National Aerospace Laboratory NLR to the 'CFD Drag Prediction Workshop' organized by the AIAA in Anaheim, CA, on June 9-10, 2001, has been presented. Two methods to obtain the drag coefficients have been discussed. The first method extrapolates the drag coefficient to zero mesh width from a sequence of nested grids. One should, however, note that in order to obtain good results using this method, the main flow features, such as shock waves, should be well resolved on all grids used. This method yields the grid-converged drag.
The second approach to calculate the drag coefficients is the so-called 'far-field approach'. This method is applied to one grid level only. This approach decomposes the aerodynamic drag into its three 'physical' components, i.e. vortex drag, viscous drag and wave drag. A good grid quality, for example in terms of vorticity convection, is required for this method to obtain accurate results. Because of its diagnostic potential, this method is helpful to aerodynamic designers. If applied to a sequence of grids, this method yields the same grid-converged drag results as the grid convergence study for consistent RANS solvers.

Acknowledgements

The authors would like to thank S.P. Spekreijse and H.A. Sytsma of NLR for their support in making the 'NLR' grid and J.C. Kok of NLR for his support in using the NLR ENFLOW flow solver.

References

1. AGARD A selection of experimental test cases for the validation of CFD codes. *AGARD-AR-303*, 1994.
2. BEEK, C.M. VAN, SPEKREIJSE, S.P. AND L. PAPARONE Description of theory and user's guide of AIRDRAG: a computer code for the computation of vortex, viscous and wave drag of airplane configurations. *NLR-TR* **2001-241**, 2001.
3. KOK, J.C. Resolving the dependence on free-stream values for the k-ω turbulence model. *AIAA-journal* **38-7**, 2000, 1292–1295.
4. KOK, J.C. Numerical design of ENSOLV version 3.20. A flow solver for 3D Euler/Navier-Stokes equations in arbitrary multi-block domains. *NLR-CR* **2000-620**, 2000.
5. LABAN, M. Aircraft drag and thrust analysis (AIRDATA) project overview and key results. In: Workshop on EU-Research on aerodynamic engine/aircraft integration for transport aircraft. 26-27 September 2000, DLR Braunschweig, Germany, 9.1–9.15.
6. OSKAM, B. AND J.W. SLOOFF Recent advances in computational aerodynamics at NLR. *AIAA* **98-0138**, 1998.
7. PASCARELLI, A. AND R. TOGNACCINI Drag and thrust bookkeeping from CFD calculations. *Technical report of the dipartimento di progettazione aeronautica*, Universita degli Studi di Napoli, to be published.
8. SPEKREIJSE, S.P. AND J.C. KOK Semi-automatic domain decomposition based on potential theory. *NLR-TP* **2000-366**, 2000.
9. WILCOX, D.C. Reassessment of the scale-determining equation for advanced turbulence models. *AIAA-journal* **26-11**, 1988, 1299–1310.
10. WILCOX, D.C. A two-equation turbulence model for wall-bounded and free-shear flows. *AIAA* **93-2905**, 1993.

grid	α [°]	C_L	C_D	$C_{D_{pressure}}$	$C_{D_{friction}}$	C_M
'DPW'	−0.350	0.49980	0.03049	0.01676	0.01373	−0.1671
'NLR'	−0.199	0.50013	0.02910	0.01551	0.01359	−0.1568
			0.00139	0.00125	0.00014	

Table 3 Results of test case 1 ($M_\infty = 0.75$ and $C_L = 0.500 \pm 0.001$) on the 'DPW' and 'NLR' grid (h=1).

α [°]	C_L	C_D	$C_{D_{pressure}}$	$C_{D_{friction}}$	C_M
−3	0.16192	0.02080	0.00708	0.01373	−0.1657
−2	0.28395	0.02259	0.00887	0.01372	−0.1643
−1	0.40428	0.02563	0.01196	0.01367	−0.1614
0	0.52430	0.03014	0.01658	0.01357	−0.1552
1	0.65150	0.03803	0.02462	0.01341	−0.1489
2	0.77300	0.05155	0.03835	0.01320	−0.1448

Table 4 Results of test case 2: drag polar ($M_\infty = 0.75$) on the 'NLR' grid (h=1).

M_∞	grid	α [°]	C_L	C_D	$C_{D_{pressure}}$	$C_{D_{friction}}$	C_M
0.50	'DPW'	0.298	0.49968	0.02870	0.01413	0.01456	−0.1400
	'NLR'	0.581	0.49991	0.02804	0.01369	0.01435	−0.1276
				0.00066	0.00045	0.00021	
0.60	'DPW'	0.093	0.49992	0.02883	0.01453	0.01429	−0.1480
	'NLR'	0.352	0.49996	0.02820	0.01410	0.01410	−0.1359
				0.00063	0.00043	0.00019	
0.70	'DPW'	−0.183	0.49981	0.02943	0.01548	0.01395	−0.1593
	'NLR'	0.035	0.50000	0.02868	0.01490	0.01377	−0.1477
				0.00075	0.00058	0.00018	
0.75	'DPW'	−0.350	0.49977	0.03049	0.01676	0.01373	−0.1671
	'NLR'	−0.199	0.50013	0.02910	0.01551	0.01359	−0.1568
				0.00139	0.00125	0.00014	
0.76	'DPW'	−0.394	0.49978	0.03072	0.01704	0.01367	−0.1693
	'NLR'	−0.262	0.50001	0.02916	0.01561	0.01355	−0.1594
				0.00156	0.00143	0.00012	
0.77	'DPW'	−0.442	0.49978	0.03098	0.01737	0.01362	−0.1719
	'NLR'	−0.330	0.50001	0.02927	0.01577	0.01351	−0.1625
				0.00171	0.00160	0.00011	
0.78	'DPW'	−0.496	0.49982	0.03135	0.01779	0.01355	−0.1754
	'NLR'	−0.405	0.50001	0.02945	0.01600	0.01346	−0.1664
				0.00190	0.00179	0.00009	
0.80	'DPW'	−0.537	0.49987	0.03390	0.02054	0.01336	−0.1819
	'NLR'	−0.517	0.50002	0.03158	0.01827	0.01331	−0.1767
				0.00232	0.00227	0.00005	

Table 5 Results of test case 3: constant-C_L-Mach-sweep ($C_L = 0.500 \pm 0.001$) on the 'DPW' grid and the 'NLR' grid (h=1).

M_∞	α [°]	C_L	C_D	$C_{D_{pressure}}$	$C_{D_{friction}}$	C_M
0.50	−0.468	0.40010	0.02466	0.01025	0.01441	−0.1355
0.60	−0.639	0.40008	0.02478	0.01062	0.01417	−0.1428
0.70	−0.874	0.40007	0.02514	0.01128	0.01386	−0.1535
0.75	−1.035	0.40005	0.02550	0.01183	0.01367	−0.1615
0.76	−1.074	0.40004	0.02560	0.01198	0.01363	−0.1636
0.77	−1.118	0.40004	0.02573	0.01215	0.01358	−0.1660
0.78	−1.161	0.40004	0.02601	0.01248	0.01353	−0.1688
0.80	−1.232	0.40002	0.02717	0.01377	0.01340	−0.1753

Table 6 Results of test case 4: Mach/C_L-matrix (Drag rise curve) ($C_L = 0.400$) on the 'NLR' grid (h=1).

M_∞	α [°]	C_L	C_D	$C_{D_{pressure}}$	$C_{D_{friction}}$	C_M
0.50	0.581	0.49991	0.02804	0.01369	0.01435	−0.1276
0.60	0.352	0.49996	0.02820	0.01410	0.01417	−0.1359
0.70	0.035	0.50000	0.02868	0.01490	0.01377	−0.1477
0.75	−0.199	0.50013	0.02910	0.01551	0.01359	−0.1568
0.76	−0.262	0.50001	0.02916	0.01561	0.01355	−0.1594
0.77	−0.330	0.50001	0.02927	0.01577	0.01351	−0.1625
0.78	−0.405	0.50001	0.02945	0.01600	0.01346	−0.1664
0.80	−0.517	0.50002	0.03158	0.01827	0.01331	−0.1767

Table 7 Results of test case 4: Mach/C_L-matrix (Drag rise curve) ($C_L = 0.500 \pm 0.001$) on the 'NLR' grid (h=1).

M_∞	α [°]	C_L	C_D	$C_{D_{pressure}}$	$C_{D_{friction}}$	C_M
0.50	1.639	0.59968	0.03232	0.01805	0.01426	−0.1189
0.60	1.357	0.59977	0.03256	0.01857	0.01399	−0.1277
0.70	0.970	0.59990	0.03387	0.02021	0.01366	−0.1383
0.75	0.603	0.59998	0.03425	0.02078	0.01348	−0.1508
0.76	0.508	0.59999	0.03439	0.02096	0.01343	−0.1551
0.77	0.410	0.59999	0.03473	0.02135	0.01338	−0.1604
0.78	0.319	0.59999	0.03558	0.02226	0.01332	−0.1667
0.80	0.284	0.59998	0.04038	0.02723	0.01315	−0.1770

Table 8 Results of test case 4: Mach/C_L-matrix (Drag rise curve) ($C_L = 0.600 \pm 0.001$) on the 'NLR' grid (h=1).

	'DPW' grid		'NLR' grid			
	h=2	h=1	h=4	h=2	h=4/3	h=1
C_D	0.03919	0.03263	0.04568	0.03360	0.03112	0.03014
$C_{D_{pressure}}$	0.02480	0.01894	0.03192	0.01979	0.01746	0.01658
$C_{D_{friction}}$	0.01440	0.01369	0.01376	0.01381	0.01367	0.01357

Table 9 Drag data for $M_\infty = 0.75$ and $\alpha = 0°$ on the 'DPW' grid and the 'NLR' grid.

	'DPW' grid				
	h=2	h=1	h=0		
C_D (Eq. 1)					
C_D (Eq. 1)					
C_D (Eq. 2)	0.03919	0.03263	0.02904		
C_D (Eq. 2)					
	'NLR' grid				
	h=4	h=2	h=4/3	h=1	h=0
C_D (Eq. 1)	0.04568	0.03360		0.03014	0.02841
C_D (Eq. 1)		0.03360	0.03112	0.03014	0.02827
C_D (Eq. 2)		0.03360		0.03014	0.02825
C_D (Eq. 2)			0.03112	0.03014	0.02834

Table 10 Grid convergence study for $M_\infty = 0.75$ and $\alpha = 0°$ on the 'DPW' grid and the 'NLR' grid (see also Tab. 1).

grid	$x_{Trefftz}$ (mm)	$C_{D_{vortex}}$	$C_{D_{wave}}$	$C_{D_{viscous}}$	$C_{D_{far\text{-}field}}$
'DPW'	2400	0.00950	0.00020	0.01928	0.02898
'DPW'	1250	0.01050	0.00019	0.01909	0.02978
'NLR'	2400	0.00792	0.00010	0.01876	0.02678
'NLR'	1250	0.00963	0.00010	0.01979	0.02952

Table 11 Total drag breakdown data for $M_\infty = 0.75$ and $\alpha = 0°$ on the 'NLR' grid (h=1).

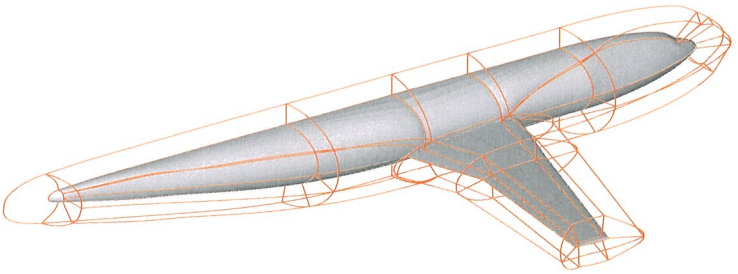

Fig. 1(a) Domain decomposition around the DLR-F4 wing body configuration using the domain modeler ENDOMO, part of the ENFLOW CFD system: the first layer of blocks around the configuration generated using the 'off-set' method. Red lines indicate the block boundaries.

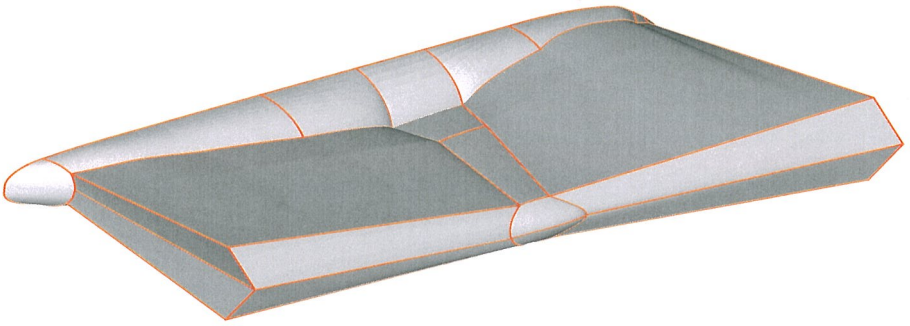

Fig. 1(b) Domain decomposition around the DLR-F4 wing body configuration using the domain modeler ENDOMO, part of the ENFLOW CFD system: the first layer of blocks around the configuration plus the additional blocks to make this layer more convex, as needed for the 'potential' method. Red lines indicate the block boundaries.

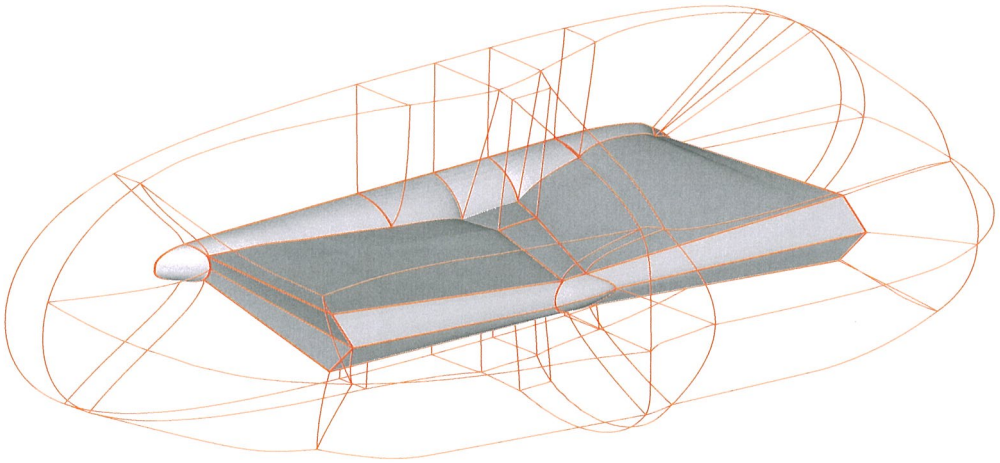

Fig. 1(c) Domain decomposition around the DLR-F4 wing body configuration using the domain modeler ENDOMO, part of the ENFLOW CFD system: the second layer of blocks around the configuration generated by the 'potential' method. Red lines indicate the block boundaries.

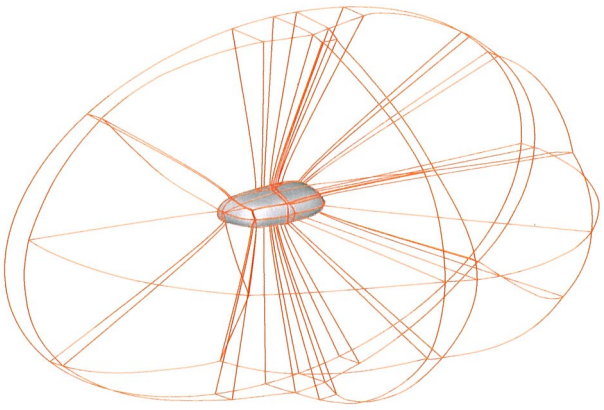

Fig. 1(d) Domain decomposition around the DLR-F4 wing body configuration using the domain modeler ENDOMO, part of the ENFLOW CFD system: the third layer of blocks generated by the 'potential' method. Red lines indicate the block boundaries.

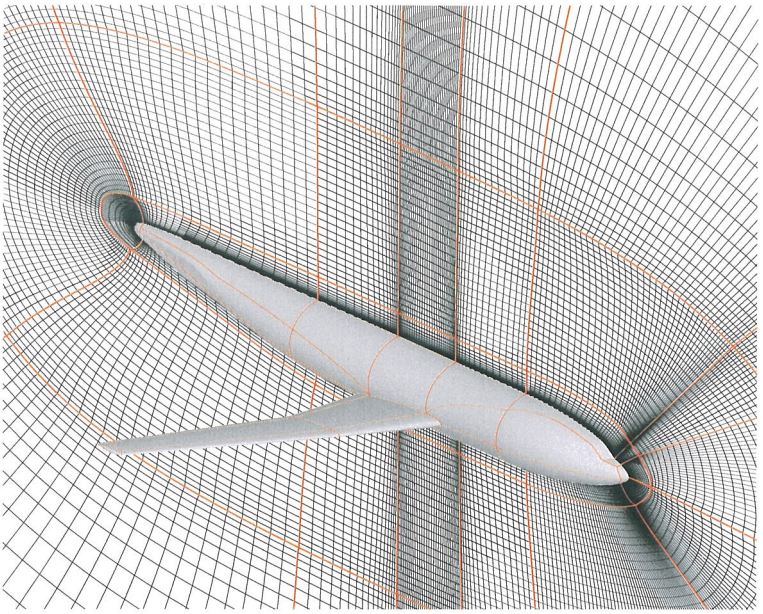

Fig. 2(a) Grid in the symmetry plane for the 'NLR' grid (h=1) around the DLR-F4 wing/body configuration. Red lines indicate the block boundaries.

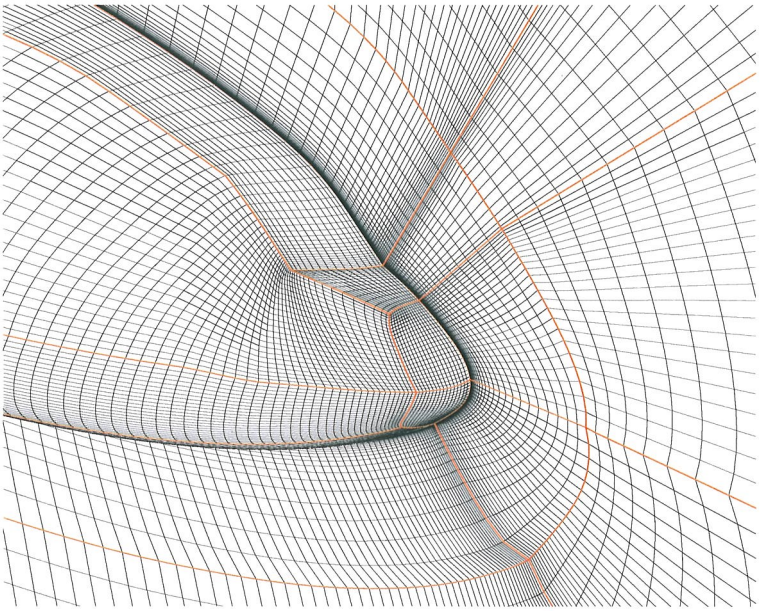

Fig. 2(b) Grid around the nose for the 'NLR' grid (h=1) around the DLR-F4 wing/body configuration. Red lines indicate the block boundaries.

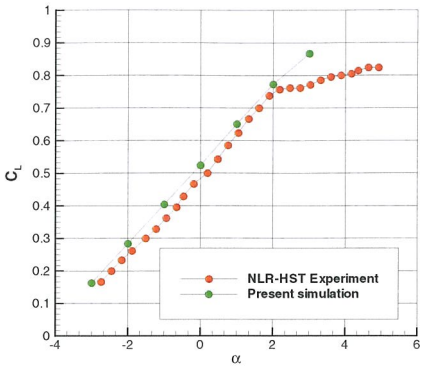

Fig. 3(a) C_L-α-curve for $M_\infty = 0.75$ on the 'NLR' grid (h=1). Note that also data for $\alpha = 3°$ is included.

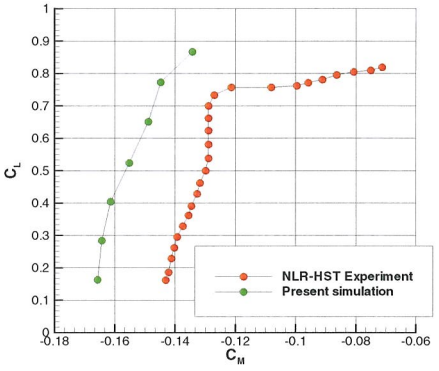

Fig. 3(b) C_L-C_M-curve for $M_\infty = 0.75$ on the 'NLR' grid (h=1). Note that also data for $\alpha = 3°$ is included.

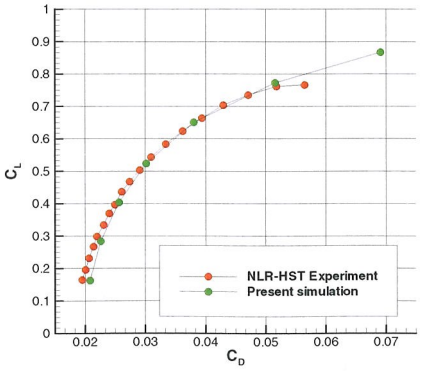

Fig. 3(c) C_L-C_D-curve for $M_\infty = 0.75$ on the 'NLR' grid (h=1). Note that also data for $\alpha = 3°$ is included.

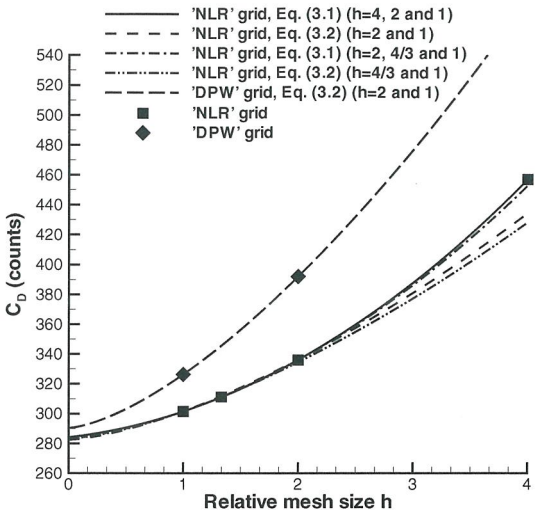

Fig. 4(a) Aerodynamic drag extrapolation on the 'DPW' grid (h=2 and 1) and the 'NLR' grid (h=4, 2, 4/3 and 1) for $M_\infty = 0.75$ and $\alpha = 0°$ (see also Tab. 1).

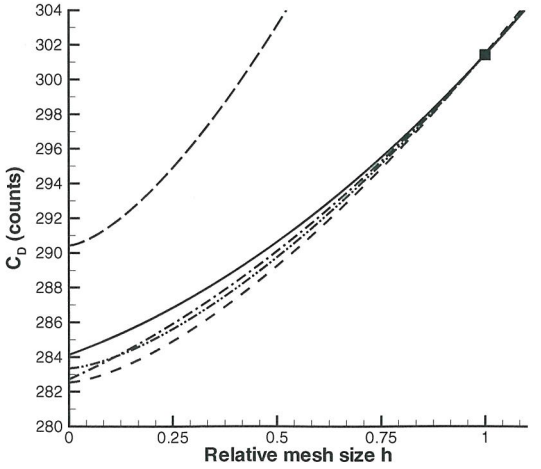

Fig. 4(b) Detail of the aerodynamic drag extrapolation on the 'DPW' grid (h=2 and 1) and the 'NLR' grid (h=4, 2, 4/3 and 1) for $M_\infty = 0.75$ and $\alpha = 0°$ (see also Tab. 1).

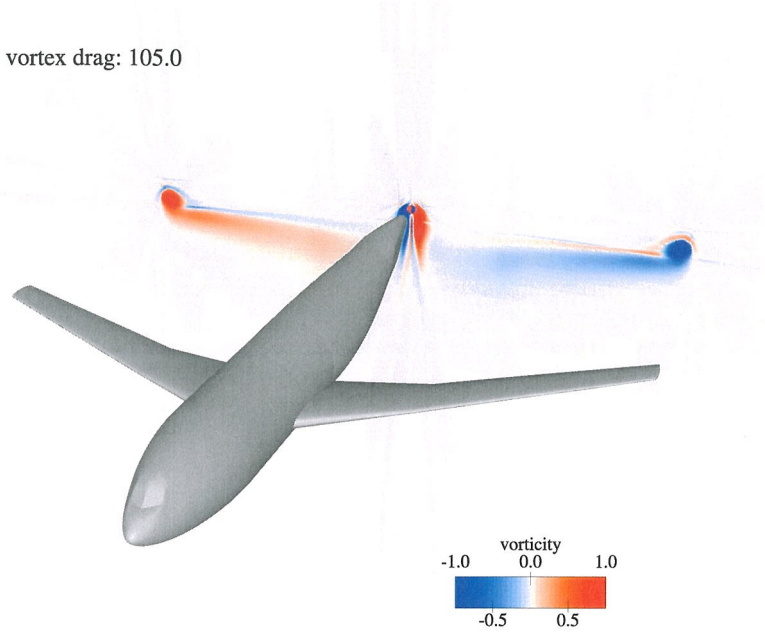

Fig. 5(a) Total drag breakdown on the 'DPW' grid (h=1) for $M_\infty = 0.75$, $\alpha = 0°$ and $x_{Trefftz} = 1250$ mm: vorticity distribution on the 'Trefftz plane'.

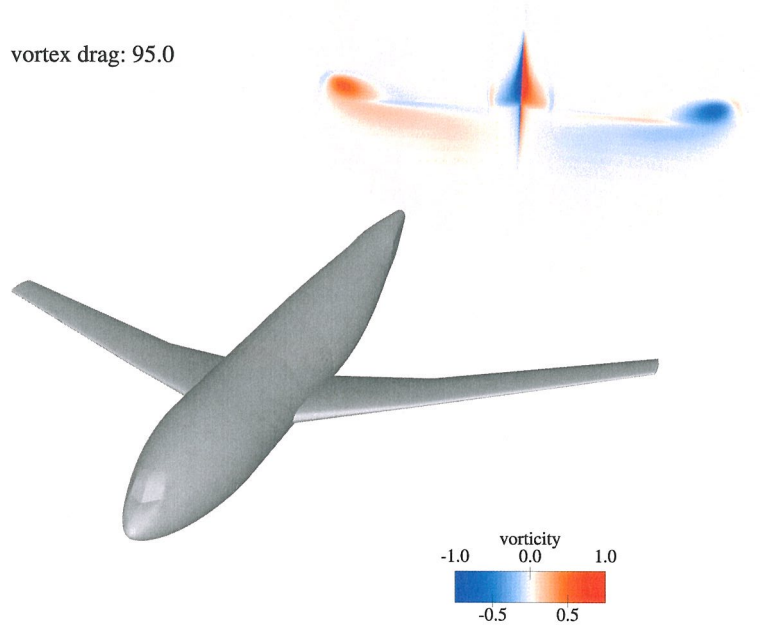

Fig. 5(b) Total drag breakdown on the 'DPW' grid (h=1) for $M_\infty = 0.75$, $\alpha = 0°$ and $x_{Trefftz} = 2400$ mm: vorticity distribution on the 'Trefftz plane'.

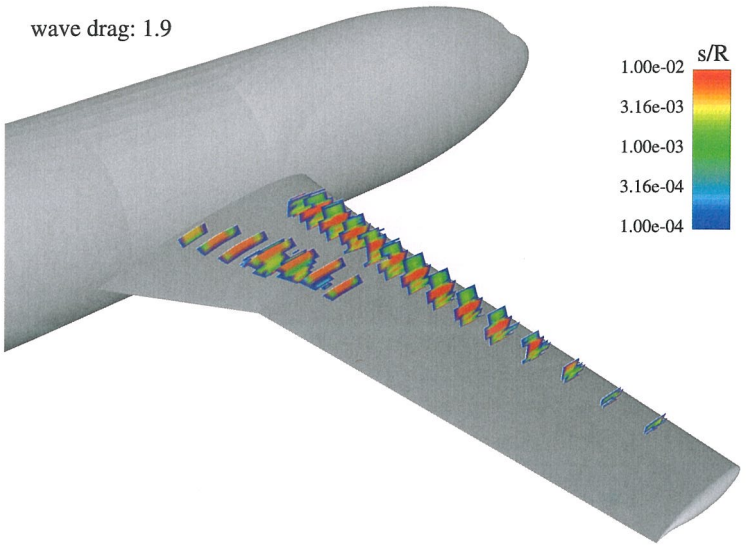

Fig. 5(c) Total drag breakdown on the 'DPW' grid (h=1) for $M_\infty = 0.75$, $\alpha = 0°$ and $x_{Trefftz} = 1250$ mm: wave drag cells extracted from grid cell entropy production in shock region.

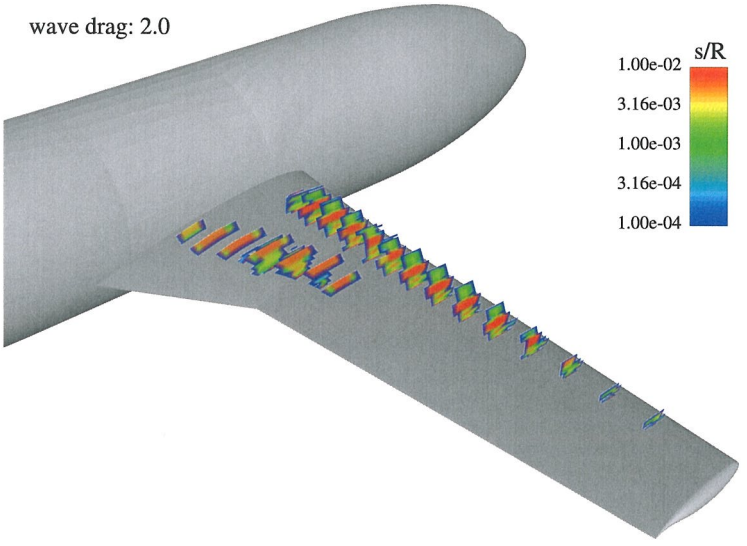

Fig. 5(d) Total drag breakdown on the 'DPW' grid (h=1) for $M_\infty = 0.75$, $\alpha = 0°$ and $x_{Trefftz} = 2400$ mm: wave drag cells extracted from grid cell entropy production in shock region.

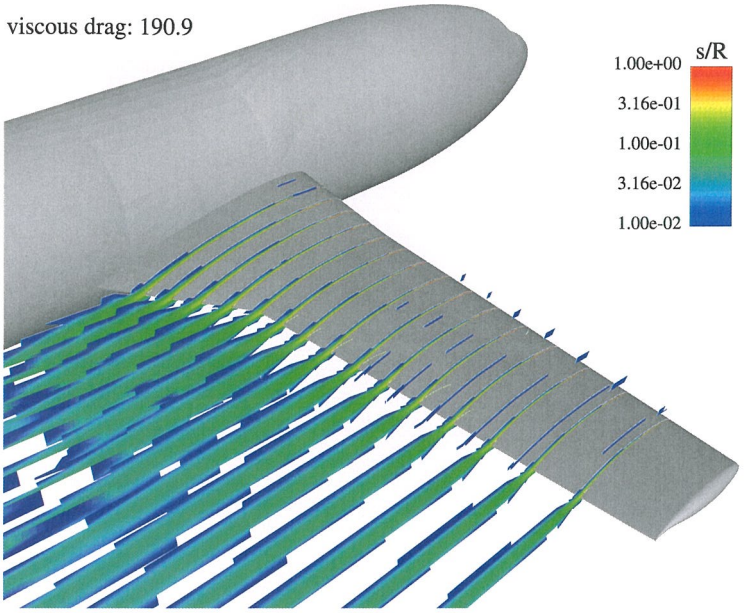

Fig. 5(e) Total drag breakdown on the 'DPW' grid (h=1) for $M_\infty = 0.75$, $\alpha = 0°$ and $x_{Trefftz} = 1250$ mm: viscous drag cells extracted from grid cell entropy production in viscous region (on the wing only).

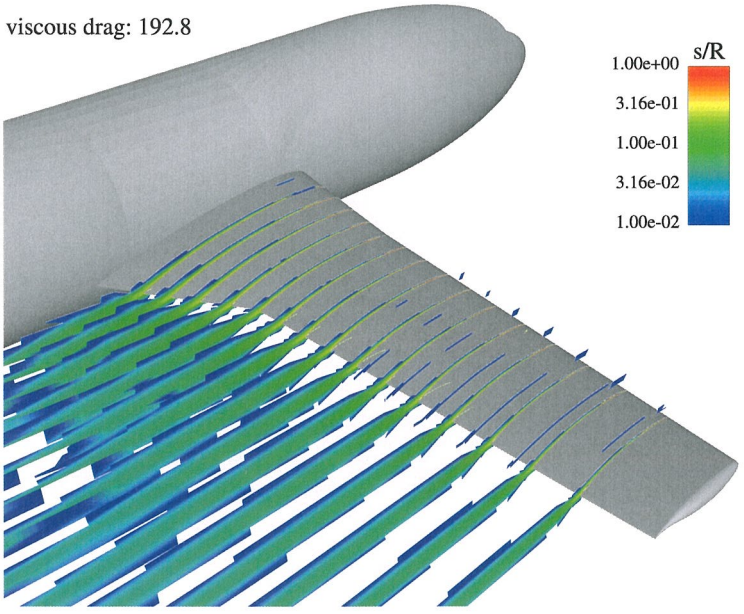

Fig. 5(f) Total drag breakdown on the 'DPW' grid (h=1) for $M_\infty = 0.75$, $\alpha = 0°$ and $x_{Trefftz} = 2400$ mm: viscous drag cells extracted from grid cell entropy production in viscous region (on the wing only).

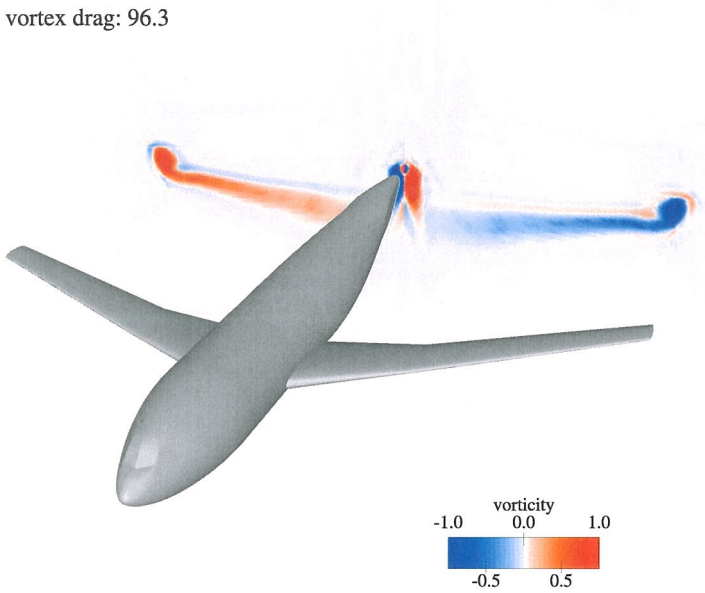

Fig. 6(a) Total drag breakdown on the 'NLR' grid (h=1) for $M_\infty = 0.75$, $\alpha = 0°$ and $x_{Trefftz} = 1250$ mm: vorticity distribution on the 'Trefftz plane'.

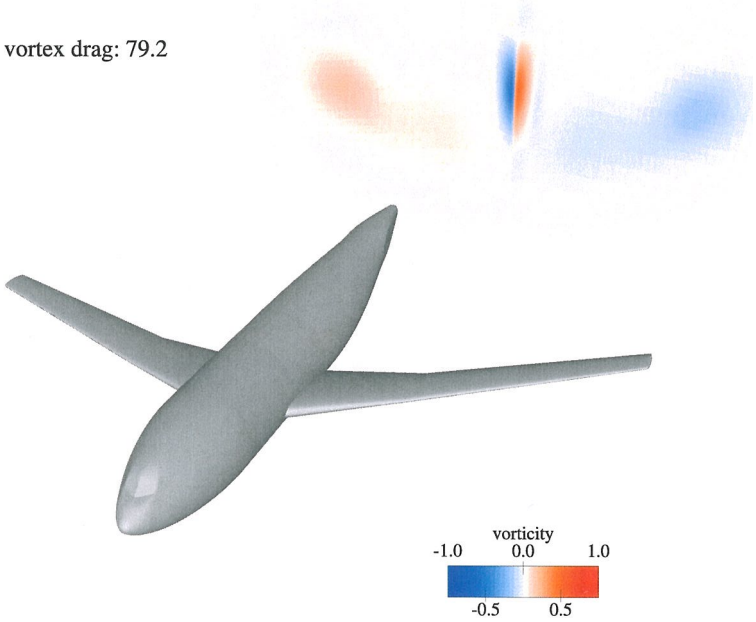

Fig. 6(b) Total drag breakdown on the 'NLR' grid (h=1) for $M_\infty = 0.75$, $\alpha = 0°$ and $x_{Trefftz} = 2400$ mm: vorticity distribution on the 'Trefftz plane'.

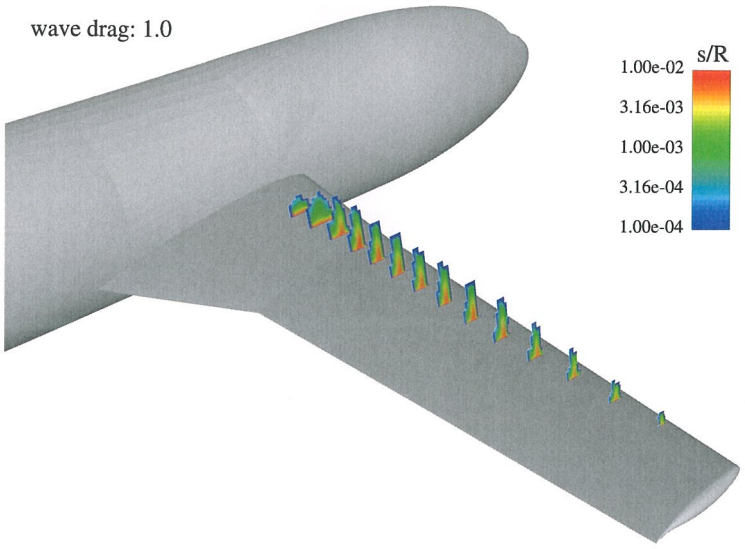

Fig. 6(c) Total drag breakdown on the 'NLR' grid (h=1) for $M_\infty = 0.75$, $\alpha = 0°$ and $x_{Trefftz} = 1250$ mm: wave drag cells extracted from grid cell entropy production in shock region).

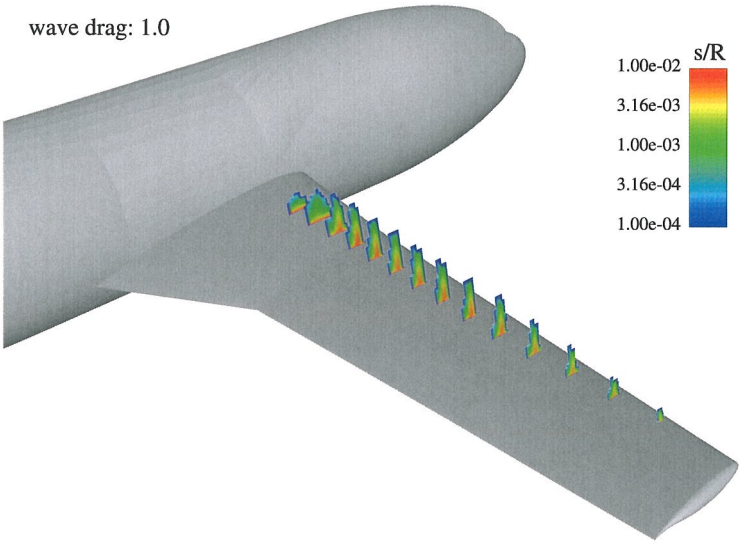

Fig. 6(d) Total drag breakdown on the 'NLR' grid (h=1) for $M_\infty = 0.75$, $\alpha = 0°$ and $x_{Trefftz} = 2400$ mm: wave drag cells extracted from grid cell entropy production in shock region.

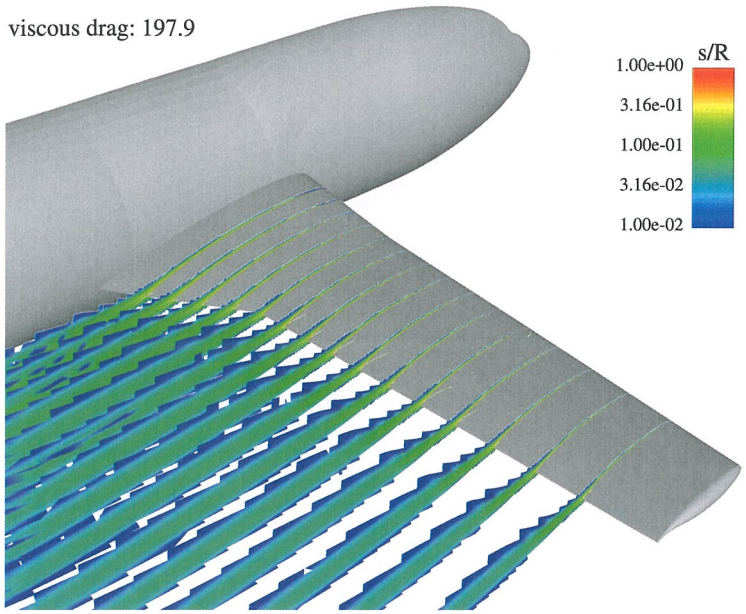

Fig. 6(e) Total drag breakdown on the 'NLR' grid (h=1) for $M_\infty = 0.75$, $\alpha = 0°$ and $x_{Trefftz} = 1250$ mm: viscous drag cells extracted from grid cell entropy production in viscous region (on the wing only).

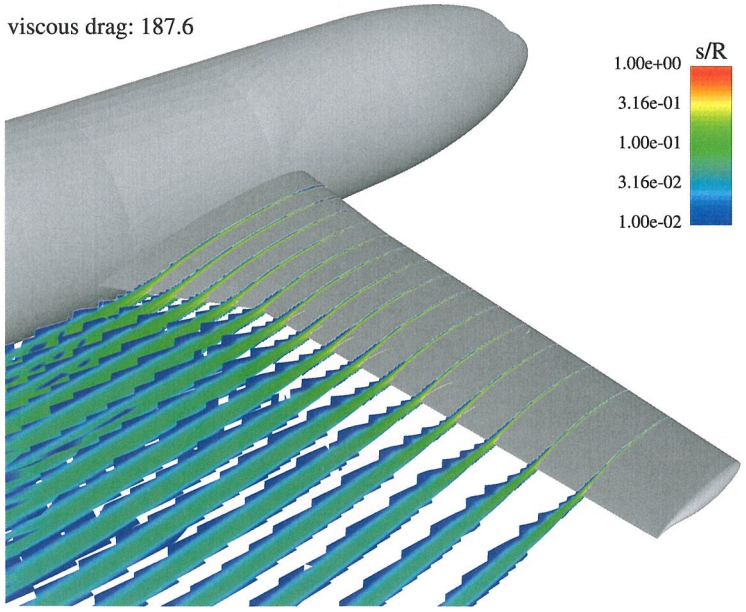

Fig. 6(f) Total drag breakdown on the 'NLR' grid (h=1) for $M_\infty = 0.75$, $\alpha = 0°$ and $x_{Trefftz} = 2400$ mm: viscous drag cells extracted from grid cell entropy production in viscous region (on the wing only).